

Label-free volumetric quantitative imaging of human osteosarcoma cells by hyperspectral coherent anti-Stokes Raman scattering

Karuna, Arnica; Masia, Francesco; Wiltshire, Marie; Errington, Rachel; Borri, Paola; Langbein, Wolfgang

DOI

[10.1117/12.2510277](https://doi.org/10.1117/12.2510277)

Publication date

2019

Document Version

Accepted author manuscript

Published in

Proceedings of SPIE

Citation (APA)

Karuna, A., Masia, F., Wiltshire, M., Errington, R., Borri, P., & Langbein, W. (2019). Label-free volumetric quantitative imaging of human osteosarcoma cells by hyperspectral coherent anti-Stokes Raman scattering. In A. Periasamy, P. T. C. So, & K. König (Eds.), *Proceedings of SPIE: Multiphoton Microscopy in the Biomedical Sciences XIX* (Vol. 10882). Article 108821P (MULTIPHOTON MICROSCOPY IN THE BIOMEDICAL SCIENCES XIX). SPIE. <https://doi.org/10.1117/12.2510277>

Important note

To cite this publication, please use the final published version (if applicable). Please check the document version above.

Copyright

Other than for strictly personal use, it is not permitted to download, forward or distribute the text or part of it, without the consent of the author(s) and/or copyright holder(s), unless the work is under an open content license such as Creative Commons.

Takedown policy

Please contact us and provide details if you believe this document breaches copyrights. We will remove access to the work immediately and investigate your claim.

Label-free volumetric quantitative imaging of human osteosarcoma cells by hyperspectral coherent anti-Stokes Raman scattering

Arnica Karuna^{a,d}, Francesco Masia^a, Marie Wiltshire^b, Rachel Errington^b, Paola Borri^c, and Wolfgang Langbein^a

^aSchool of Physics and Astronomy, Cardiff University, The Parade, Cardiff CF24 3AA, United Kingdom

^bDivision of Cancer and Genetics, School of Medicine, Cardiff University, Heath park, Cardiff CF14 4XN, United Kingdom

^cSchool of Biosciences, Cardiff University, Museum Avenue, Cardiff CF10 3AX, United Kingdom

^dCurrent address: Department of Imaging Physics, Delft University of Technology, Lorentzweg 1, 2628 CJ Delft, The Netherlands

ABSTRACT

Quantitative determination of the chemical composition of unstained samples, non-invasively, with high three-dimensional spatio-temporal resolution, will accelerate progress in cell biology. The current state of the art in bioimaging is dominated by either chemically non-specific or invasive methods. In this work, we demonstrate label-free, non-invasive quantitative volumetric imaging of human osteosarcoma cells using coherent anti-Stokes Raman scattering microscopy. A data analysis method developed in-house was applied to represent the chemical composition of the cells as volumetric three-dimensional images indicating water, proteins, DNAP (mixture of DNA and proteins), and lipids, and to determine the dry masses of the organic components with picogram resolution.

Keywords: Coherent anti-Stokes Raman scattering microscopy, CARS, label-free imaging, coherent Raman scattering

1. INTRODUCTION

Studies on biological materials such as cells and tissues primarily employ optical microscopy. Imaging methods like bright-field, differential interference contrast (DIC), or dark-field microscopy reveal morphological details, but are not chemically specific. By introducing extraneous materials such as quantum dots or fluorescent labels in the samples, it is possible to gain targeted chemical specificity as well as improve the structural contrast in biological samples, which are mostly transparent to visible light. While popular in bioimaging applications, fluorescence microscopy¹⁻³ suffers from undesirable issues of photobleaching and phototoxicity. Spectroscopy techniques such as spontaneous Raman scattering microscopy provide label-free, chemically specific sub-cellular resolution for imaging applications. However, the small spontaneous Raman scattering cross-sections (10^{-29} cm²) of the molecules⁴ mandate long acquisition times and/or higher excitation powers for imaging, which can be incompatible with living biological samples. Moreover, Raman microscopy is affected by autofluorescence background from typical biological samples, limiting its present applicability to volumetric imaging and rendering it mostly incompatible with fluorescent labelling. In coherent Raman scattering microscopy (CRS), the sample molecules are coherently driven by two excitation beams, resulting in a signal enhancement of up to 10^{10} in pure materials such as lipids.⁴ As a result, imaging with CRS can work with significantly shorter acquisition times than in spontaneous Raman microscopy. CRS can be measured as coherent anti-Stokes Raman scattering

Further author information: (Send correspondence to Wolfgang Langbein)

Wolfgang Langbein: E-mail: langbeinww@cardiff.ac.uk, Telephone: +44 29 2087 0172

(CARS),⁵ or stimulated Raman scattering (SRS).⁶ Compared to SRS, CARS is easier to implement because the CARS signal is blue-shifted from the excitation beams and autofluorescence, allowing for its discrimination using band-pass filters. However, CARS signals require a more complex data processing due to the contribution of vibrationally non-resonant backgrounds. Described as $I_C \propto |\chi|^2 = |\chi_R + \chi_{NR}|^2$, the CARS intensity comprises vibrationally resonant (χ_R) and non-resonant (χ_{NR}) components of the third-order susceptibility corresponding to the CARS process. While χ_R has both real and imaginary parts, χ_{NR} is due to an electronic contribution, and is real for materials (example water, proteins, DNA, and lipids) without two-photon absorption for excitation pulses in the biological window⁴ (700-1300) nm. Therefore, $I_C \propto |\chi_R|^2 + 2\Re(\chi_R\chi_{NR}) + |\chi_{NR}|^2$. The imaginary component of the resonant CARS susceptibility, i.e. $\Im(\chi) = \Im(\chi_R)$ resembles the spontaneous Raman scattering cross-section, with peaks at the vibrational frequencies, and is linear in the concentration of the detected chemical species. Therefore it is the quantity of interest in a quantitative CARS analysis. The challenge in retrieving $\Im(\chi)$ from the CARS intensity is the determination of the phase of χ . At the same time, this non-resonant contribution is also an advantage, as it enhances the intensity of weak χ_R by the homodyning in the interference term $2\Re(\chi_R\chi_{NR})$, and it allows to use a non-resonant material as reference for quantitative analysis.⁷ For phase retrieval, equivalent techniques⁸ in current practice are based on a time-domain Kramers-Kronig (KK) formulation⁹ and the maximum entropy method.¹⁰ We have developed a phase-corrected KK approach (PCKK) which improves on the KK formulation by correcting not only the phase but also the amplitude of the signal, and results in a quantitative susceptibility in units of χ_{ref} , relative to a known non-resonant reference material, $\bar{\chi} = \chi/\chi_{\text{ref}}$.¹¹ Glass is a suitable reference material for frequencies above 1200 cm⁻¹, and is convenient since it is typically part of the sample mount. For a larger frequency range, NaCl is a suitable choice as reference.⁷

Once the complex susceptibility is obtained, the resulting hyperspectral images have to be analysed in terms of the chemical composition of the specimen as spatially resolved maps of a few spectral components. For this step, various techniques have been proposed in literature, including classical least squares analysis,¹² independent component analysis,¹³ and multivariate curve resolution analysis.¹⁴ Our algorithm developed in-house, called FSC³ (factorization into spectra and concentrations of chemical components)^{11,15} determines quantitative spectra and absolute concentration images of separate chemical components without prior knowledge of the sample composition. We factorize the hyperspectral data as $\mathbf{D} = \sum_i \mathbf{C}_i \times \mathbf{S}_i + \mathbf{E}$, with the non-negative concentration distribution, \mathbf{C}_i and spectrum of the i -th component, \mathbf{S}_i . \mathbf{E} is the error, the norm of which is minimized. As proof of principle, this method was shown suitable for quantitative determination of the absolute volume of chemical components in three-dimensional imaging, using polystyrene beads.⁷ Recently, this technique was used to quantitatively describe various biological samples,¹⁶ study the human cell division,¹⁷ measure the lipid uptake in human adipose derived stem cells,¹⁸ to investigate the differentiation of stem cells,¹⁹ and towards high-throughput imaging using a Bessel beam and sparse sampling.²⁰

A fundamental process underlying the proliferation of cell populations, the cell cycle has been studied using methods such as fluorescence microscopy,²¹ quantitative phase contrast,^{22,23} and DIC.²⁴ These methods are either invasive (introduction of extraneous labels as in fluorescence microscopy) or lack chemical specificity. The cell cycle comprises two stages, interphase and mitosis. Recently, we reported a quantitative study of mitosis in human cells using chemically specific, label-free hyperspectral CARS microscopy.¹⁷ Briefly, the dry masses of various biomolecules, namely, proteins, a mixture of DNA and proteins, which we call here DNAP, and lipids were calculated over the whole cell and in the chromosomal regions. The attribution of the FSC³ components to various cell compartments/biomolecules was validated using fluorescence labelling of the cells with well-characterized fluorophores, DAPI and Mitotracker-orange. Furthermore, cells treated with Taxol were also studied, revealing hyperproteic and hyperlipidic effects of drug treatment. In this work, we demonstrate the application of our method to quantitatively describe cells in the interphase stage of the cell cycle, using hyperspectral CARS microscopy.

2. METHODS

2.1 Sample preparation

Fixed human osteosarcoma cells [U-2 OS] (ATCC HTB-96) transfected with a G2M Cell Cycle Phase Marker (GE Healthcare, UK) were used in this study. The cells were cultured as described in Ref. 17, and seeded on #1 coverslips placed into a single well of a multi-well plate. They were allowed to adhere and proliferate for 24

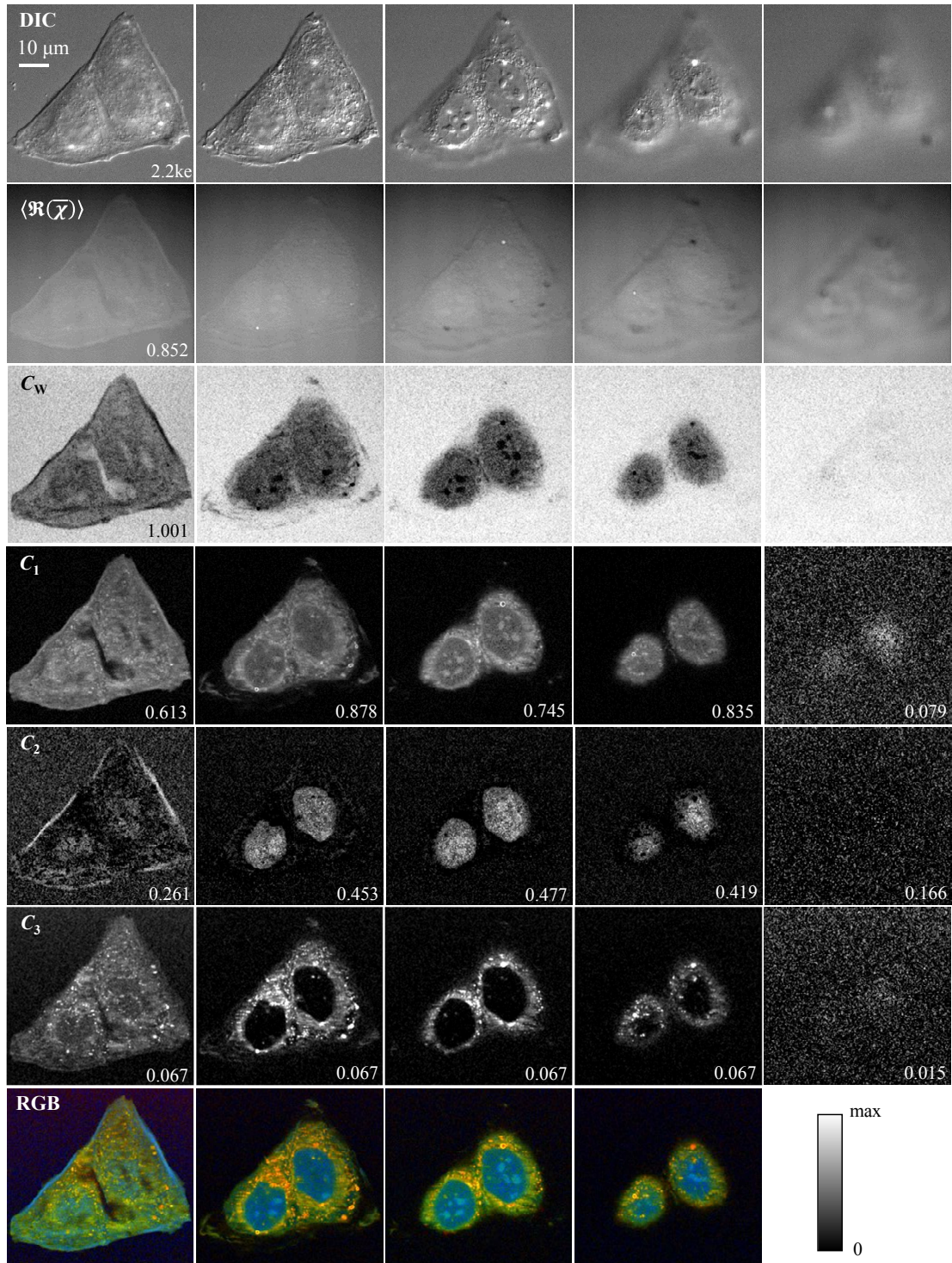


Figure 1. DIC and CARS microscopy of U-2 OS cells in interphase. Images are xy sections at progressing z -positions in steps of $2\mu\text{m}$ from left to right. The different rows show the DIC images (top), followed by $\langle \Re(\bar{\chi}) \rangle$ and FSC³ components W, 1, 2, and 3 corresponding to sum water, protein, DNAP, and lipid respectively. The grayscale is from 0 (black) to a maximum (white) value as indicated. Some scales are saturated to allow for better contrast, the maximum of DIC images is 12.2ke, and the maximum concentrations in C_1 is 0.878, C_2 is 0.478, and C_3 is 0.727. The lowermost row shows an overlay of components 1, 2, and 3 in green, blue, and red respectively.

hours, in complete TC media comprising McCoys media, 10% fetal bovine serum (FBS), Penicillin/Streptomycin, Glutamine and G418. After washing with PBS, the cells were fixed for 30 minutes in 4% paraformaldehyde (PFA). The samples were stored up to 48 hours in phosphate buffer saline (PBS). The well-plates were covered and refrigerated at 4°C until imaging. To mount the cells for imaging, approximately 13 μL PBS was pipetted into the 13 mm diameter opening of a 0.12 mm thick adhesive imaging spacer (Grace Biolabs Secure Seal) on a 1 mm microscope slide. The coverslip was then inverted over the medium filled well on the slide, ready to be imaged.

2.2 Imaging

The data presented in this work were acquired on a home-built multi-modal inverted microscope set-up^{7,25} built around a Nikon Ti-U. Briefly, we split the broadband output (660–970 nm) from a 5 fs Ti:Sapphire laser (Venteon Pulse One PE) with 80 MHz repetition rate into a pump beam (660–730) nm, a Stokes beam (730–900) nm, and a beam for two-photon excitation (TPE) (900–970) nm. The TPE beam is negatively pre-chirped using a SF59 prism compressor to achieve 30 fs pulses at the sample. Spectral focussing^{26,27} was implemented, which applies an equal linear chirp to both pump and Stokes beams to obtain a constant, tunable instantaneous frequency difference (IFD) with an adjustable pulse duration and thus spectral resolution. The chirp is created simply using SF57 glass blocks of selectable thickness in addition to the other dispersive optical elements (in particular the microscope objective lens) in the beam path. The IFD is tuned by varying the time delay between pump and Stokes beams. The IFD resolution is about 20 cm^{-1} given by the 1.6 ps pump pulse duration, with the Stokes pulse being significantly longer. The three-dimensional data presented in this paper were acquired using a 60 \times 1.27 NA water immersion objective (Nikon CFI Plan Apochromat IR λS series) and a 1.34 NA oil immersion condenser. The setup also allowed to perform standard wide-field microscopy such as bright-field, epi-fluorescence, and differential interference contrast (DIC). DIC microscopy was used to select cells for imaging with CARS. The hyperspectral CARS images were analyzed using the hyperspectral image analysis (HIA) software developed in our group,^{7,11,15} which retrieves the complex susceptibility $\bar{\chi}$ relative to a glass reference. The volumetric images of $\bar{\chi}$ are then factorized into susceptibilities and concentrations of chemical components via FSC³ which applies a non-negativity constrain on concentrations and the imaginary part $\Im(\bar{\chi})$ as well as the spectrally averaged real part $\langle\Re(\bar{\chi})\rangle$ of the component spectra. The CARS intensity data were taken with a pixel dwell time of 1 μs , z -step size of 0.7 μm and 35 mW pump power and 27 mW Stokes power at the sample, over the spectral range (2600–3600) cm^{-1} . The susceptibility $\bar{\chi}$ was retrieved over this range, and analyzed using FSC³ over the spectral range (2750–3200) cm^{-1} . The FSC³ analysis range was restricted as such to reduce the influence of systematic errors in the dominating water component (note that the imaged volume contains >95% water), with OH-stretching resonances dominating $\Im(\bar{\chi})$ above 3200 cm^{-1} .

3. RESULTS

Fig. 1 shows two interphase cells imaged using DIC and CARS microscopy. The DIC images at various axial positions are given in the top row, showing contrast in the lipid droplets and membranes. The nuclear regions containing nucleoli are also visible. The $\langle\Re(\bar{\chi})\rangle$ (second row) is expected to be similar to a refractive index image, showing features of the cellular morphology as also observed in DIC. In the following rows, the FSC³ concentrations of the organic components corresponding to protein (\mathcal{C}_1), DNAP (\mathcal{C}_2), and lipid (\mathcal{C}_3) are shown. In addition to these organic components, we define a sum water component \mathcal{C}_W with concentration given by the sum of the concentrations of the water components ($\mathcal{C}_5 - \mathcal{C}_7$ in Fig. 5), and a spectrum given by the average of their spectra weighted by their mean concentration over the imaged volume. We note that \mathcal{C}_W is homogeneous outside the cell, and has an intracellular distribution having the dry volume as negative contrast, varying across the intracellular compartments such as nuclei, nucleoli and cytosol. \mathcal{C}_1 is showing the distribution of protein, present inside the cell, specifically in the cytosol. \mathcal{C}_2 is confined to the nuclei and \mathcal{C}_3 is in the lipid droplets and membranes. The last row is a color overlay of the organic components 1-3 in green, blue, and red respectively. The z -sections of the 3D stacks corresponding to $\mathcal{C}_1, \mathcal{C}_2$ and \mathcal{C}_3 are shown in Fig. 2, with dotted lines indicating the axial positions of the slices shown in Fig. 1. The corresponding FSC³ spectra of these components are given in Fig. 3a. This analysis was using 8 FSC³ components and the remaining components $\mathcal{C}_4 - \mathcal{C}_8$ and the errors of the factorization are given in the appendix in Fig. 5. \mathcal{C}_4 is a residual organic component, $\mathcal{C}_5 - \mathcal{C}_7$ correspond to water, and \mathcal{C}_8 to glass. The spectra of $\mathcal{C}_4 - \mathcal{C}_8$ are given in Fig. 3b.

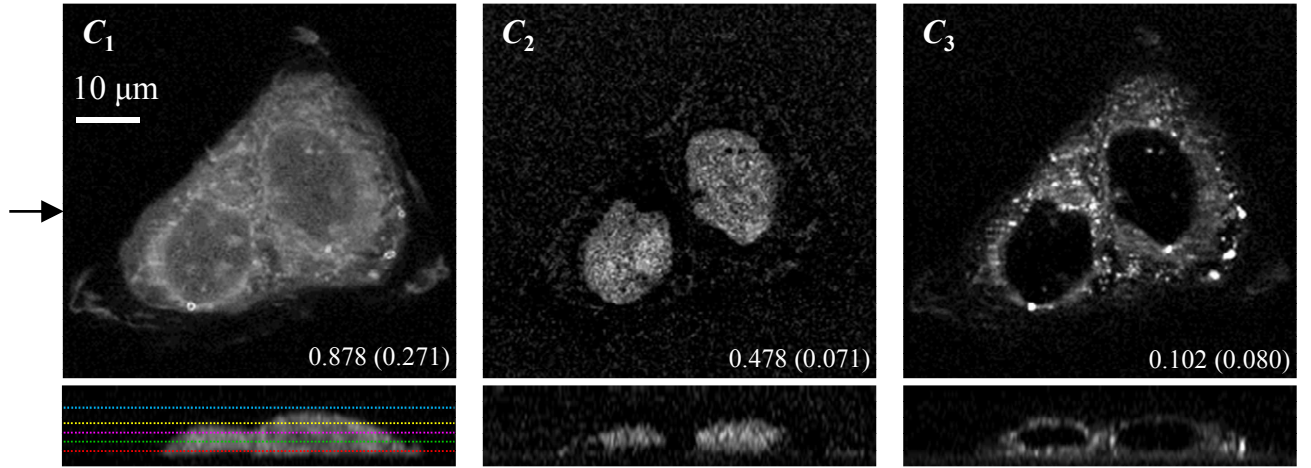


Figure 2. xy and xz sections of FSC³ concentrations of the interphase U-2OS cells shown also in Fig. 1. The grayscale minimum is 0 and the maximum is indicated. The corresponding maximum dry v/v concentration are given in parenthesis. The z positions of the xy images shown in the columns (left to right) of Fig. 1 and Fig. 5 are marked in red, green, magenta, yellow, and light blue dashed lines, respectively. The arrow indicates the position at which the z -section was taken. The xy sections shown here correspond to those in Fig. 1 second column from left (corresponding to the green dashed line), for FSC³ components 1-3.

3.1 Calculation of dry fractions and masses

As seen from their concentrations and spectra, the FSC³ components include a significant fraction of water, showing a rising $\Im(\bar{\chi})$ in the (3100–3200) cm^{-1} range, due to the large volume fraction of water in cells. Therefore, in order to quantify the dry masses of the various components, we have to remove the water. Assuming that for IFDs above 3100 cm^{-1} , $\Im(\bar{\chi})$ is dominated by the water component, while the organic components have significant $\Im(\bar{\chi})$ in the range (2800–3100) cm^{-1} , we follow the method described in Ref. 17. Briefly, we subtract a fraction α of the water spectrum $\Im(\bar{\chi}_W)$ from the component spectra, resulting in the dry spectrum $\Im(\bar{\chi}_{\text{dry}}) = \Im(\bar{\chi}) - \alpha\Im(\bar{\chi}_W)$. The choice of α is such that $\Im(\bar{\chi}_{\text{dry}})$ is zero at the upper limit of the IFD range analyzed by FSC³. The values of α and the corresponding spectra for the three organic components are shown in Fig. 4. The dry volume fractions for each FSC³ component, $\gamma_i^d = A_i/(A_{\text{OA}}F_i)$, where A_{OA} is the area integral of a measured pure dry material (here, oleic acid (OA)) and A_i is the area integral of $\Im(\bar{\chi}_{\text{dry}})$ of FSC³ component i over the CH stretch region. The hydrogen bond abundance factors, F_i account for the volume density of Raman active bonds in the IFD

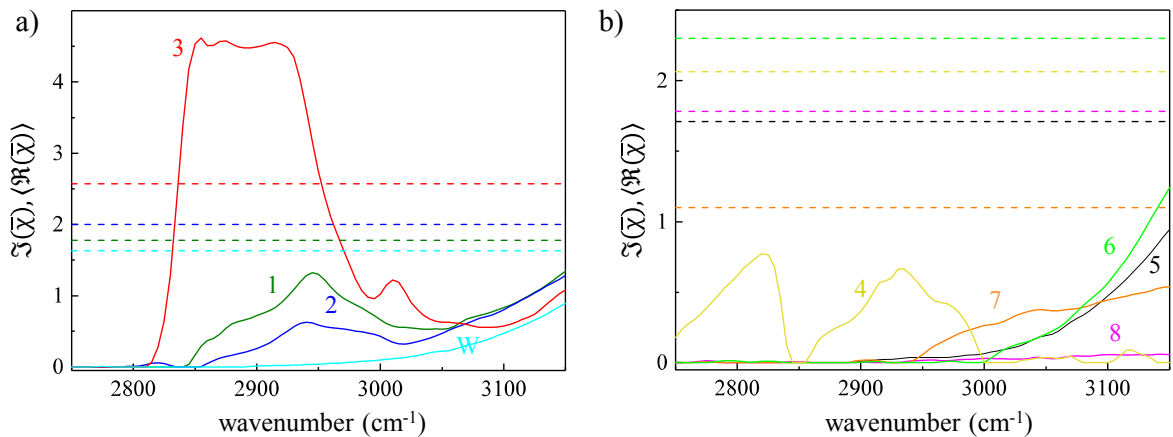


Figure 3. Spectra of FSC³ components; (a) of C_1 , C_2 , C_3 , and C_W shown in Fig. 1; (b) of $C_4 - C_8$ shown in Fig. 5. $\Im(\bar{\chi})$ is shown in solid lines while $\langle \Re(\bar{\chi}) \rangle$ is shown with dashed lines.

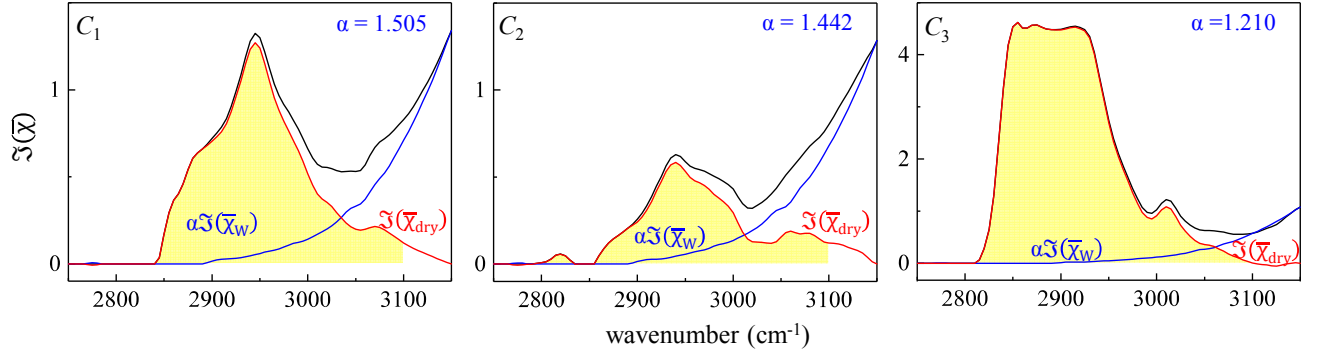


Figure 4. Estimation of dry fractions γ^d for C_1, C_2 , and C_3 of the factorization shown in Fig. 1. From $\Im(\bar{\chi})$ of C_i (black), scaled water $\alpha\Im(\bar{\chi}_w)$ (blue) is subtracted, resulting in $\Im(\bar{\chi}_{dry})$ (red) for each component. Areas of integration are shown in yellow, and result in dry areas of $A_1 = 142.89 \text{ cm}^{-1}$, $A_2 = 66.93 \text{ cm}^{-1}$, and $A_3 = 623.90 \text{ cm}^{-1}$.

range analyzed, for various FSC³ components. Mathematically,

$$F_i = \frac{b_i}{b_{OA}} \frac{m_{OA}}{m_i} \frac{\rho_i}{\rho_{OA}}$$

where b_{OA} (b_i) is the number of Raman active bonds in a molecule of OA (C_i) in the IFD range considered, m_{OA} (m_i) is the molecular weight of OA (C_i) and ρ_{OA} (ρ_i) is the mass density of OA (C_i), respectively. We use chromatin as model to describe DNAP (C_2) as a weighted average of protein and DNA in 2:1 ratio.²⁸ We calculate $F_1 = 0.58$ for proteins (C_1), $F_2 = 0.56$ for DNAP, and $F_3 = 1.0$ for lipids.

The masses of the organic FSC³ components in the cells were determined in two different regions of interest (ROI) - the nuclear region and the whole cell, defined by the visible cell morphology in C_1 and C_2 . The dry volumes V_i and masses M_i of the FSC³ components C_i were then calculated as volume integrals

$$V_i = \gamma_i^d \int_{ROI} C_i(\mathbf{r}) dV, \quad \text{and} \quad M_i = V_i \rho_i \quad (1)$$

with the three-dimensional position \mathbf{r} . The results of these volumetric calculations, divided by 2 to indicate values per cell, for the nuclear and cell ROIs, are given in Table 1. The errors given for V_i account for the error in A_i due to the selection of α and the fluctuations in the spectra.

To obtain a better separation between the protein and DNAP components, the masses M_D and M_P in Table 1 are rebalanced so that the DNAP content outside the nucleus is zero. The resulting rebalanced masses are defined as $\tilde{M}_P = M_P + \beta M_D$ and DNAP, $\tilde{M}_D = M_D - \beta M_P$, where $\beta = M_D/M_P$ with the DNAP mass M_D and

Table 1. Volumes and masses per cell of C_1, C_2 and C_3 of U-2 OS cells in interphase, over the nuclear and cell volumes. The percentage of nuclear to cell volume is indicated. The rebalanced masses \tilde{M}_P and \tilde{M}_D are given in parentheses.

i	Type	γ_i^d	$V_i(\mu\text{m}^3)$	$V_i/V_{ROI}(\%)$	$M_i(\text{pg})$
Fig. 1 - nuclear volume - $908 \mu\text{m}^3$ (18%)					
1	P	0.309	88 ± 3	9.76	114.7 (125.3)
2	D	0.149	19 ± 3	2.15	29.1 (18.6)
3	L	0.783	7.26 ± 0.03	0.80	6.5
Fig. 1 - cell volume - $4910 \mu\text{m}^3$					
1	P	0.309	277 ± 11	5.69	360.6 (393.8)
2	D	0.149	34 ± 4	0.71	51.7 (18.6)
3	L	0.783	53.8 ± 0.2	1.10	48.1

protein mass M_P in the extra-nuclear region. The resulting rebalanced masses are given in parentheses in Table 1. We note that the cell dry mass is about 450 pg, dominated by proteins (80%), followed by lipids and DNAP. Within the nuclear region, we observe a low lipid mass, which is to be expected considering that the nucleus is composed primarily of proteins and nucleic acids. Moreover, the rebalanced DNAP mass of about 19 pg is consistent with the DNA mass of 14-18 pg expected after the synthesis phase of interphase.²⁸

4. CONCLUSIONS

As previously reported in our work on mitotic cells,¹⁷ due to the spectral similarities and low concentrations of the organic content in cells, we note incomplete separation of these chemical species (proteins, DNA and lipids) into distinct FSC³ components. We observe partially mixed FSC³ components such as DNAP, necessitating the rebalancing of the component masses for enhanced quantification. Notably, lipids are detected as a well-defined component in these samples due to the high abundance of C-H bonds in lipids. The components with small $\Im(\bar{\chi})$, such as DNAP, are harder to separate,¹⁷ and appear as mixed proteins and DNA in varying fractions. Regardless of this, we believe these results are impressive due to the label-free determination of the dry masses of not only lipids, but also proteins and DNAP in non-lipid rich cells containing mostly water. In addition to the analysis presented here, CARS microscopy has also been applied to the study of mitosis and the effects of drug treatment in U-2OS cells.¹⁷ The data shown in this paper provides additional information about interphase, the stage in which the cells spend most of their time during the cell cycle.

We note that the effects of PFA fixation on cell mass and Raman spectra were found to be not significant,^{29,30} so that the results shown here should be comparable to experiments on live cells. Our work thus paves way for live cell imaging with CARS microscopy to measure the dynamics of cell components in various bio-processes/metabolism. We envision that the application of faster and high-throughput CARS^{20,31} will enable statistically significant studies. Further advantages could be gained by extending the spectral measurements to the fingerprint region which is rich with characteristic peaks of various biomolecules, and combining CARS and SRS for better sensitivity. Already in its present form, the technique is expected to provide insights also in other fields, such as material science and pharmacology.

The data presented in this work are available from the Cardiff University data archive, under the digital object identifier [10.17035/d.2019.0069352591](https://doi.org/10.17035/d.2019.0069352591).

5. ACKNOWLEDGMENTS

The CARS microscope development was supported by the UK BBSRC Research Council (grant n. BB/H006575/1). The FSC³ data analysis development was supported by the UK EPSRC Research Council (Grant No. EP/H45848/1). AK acknowledges financial support by the President's Research Scholarship programme of Cardiff University. P.B. acknowledges the UK EPSRC Research Council for her Leadership fellowship award (grant n. EP/I005072/1). W.L. acknowledges support by a Leverhulme Royal Society Research Fellowship (Grant no. LT20085). The authors thank Iestyn Pope for assistance in the data acquisition.

APPENDIX A. ADDITIONAL FSC³ COMPONENTS

The concentrations maps of the components not shown in Fig. 1, and the errors of the factorization used are given in Fig. 5.

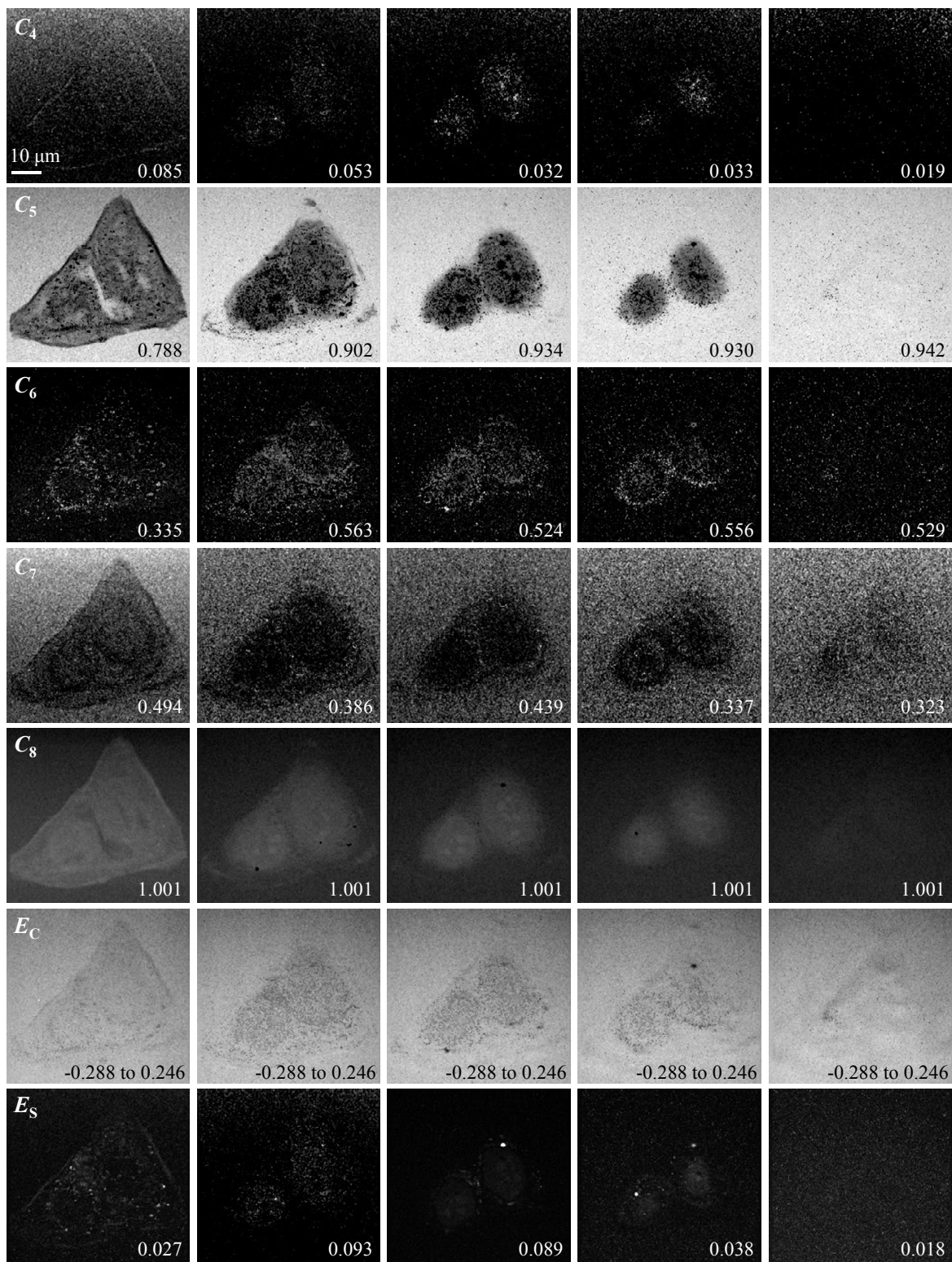


Figure 5. Concentrations of FSC³ components not shown in Fig. 1, and errors of factorization¹¹ in concentration E_C , and spectrum E_S . The grayscale is from minimum (black) to a maximum (white) value as indicated. The minimum is zero for the concentrations.

REFERENCES

- [1] Rubart, M., "Two-photon microscopy of cells and tissue," *Circ Res* **95**, 1154–1166 (2004).
- [2] Becker, W., "Fluorescence lifetime imaging- techniques and applications," *J. Microsc.* **247**, 119–136 (2012).
- [3] Chen, B.-C., Legant, W. R., Wang, K., Shao, L., Milkie, D. E., Davidson, M. W., Janetopoulos, C., Wu, X. S., Hammer, J. A., and Liu, Z., "Lattice light-sheet microscopy: Imaging molecules to embryos at high spatiotemporal resolution," *Science* **346**(6208) (2014).
- [4] Zumbusch, A., Langbein, W., and Borri, P., "Nonlinear vibrational microscopy applied to lipid biology," *Progress in Lipid Research* **52**, 615–632 (2013).
- [5] Evans, C. L. and Xie, X. S., "Coherent anti-stokes raman scattering microscopy: Chemical imaging for biology and medicine," *Annu. Rev. Anal. Chem.* **1**, 883–909 (2008).
- [6] Freudiger, C. W., Min, W., Saar, B. G., Lu, S., Holtom, G. R., He, C., Tsai, J. C., Kang, J. X., and Xie, X. S., "Label-free biomedical imaging with high sensitivity by stimulated raman scattering microscopy," *Science* **322**, 1857 (2008).
- [7] Karuna, A., Masia, F., Borri, P., and Langbein, W., "Hyperspectral volumetric coherent anti-stokes raman scattering microscopy: quantitative volume determination and nacl as non-resonant standard," *J. Raman Spectrosc.* **47**(9), 1167–1173 (2016).
- [8] Cicerone, M. T., Aamer, K. A., Lee, Y. J., and Vartiainen, E., "Maximum entropy and time-domain kramers-kronig phase retrieval approaches are functionally equivalent for cars microspectroscopy," *J. Raman Spectrosc.* **43**(5), 637–643 (2012).
- [9] Liu, Y., Lee, Y. J., and Cicerone, M. T., "Broadband cars spectral phase retrieval using a time-domain kramers-kronig transform," *Opt. Lett.* **34**, 1363 (2009).
- [10] Rinia, H. A., Bonn, M., Müller, M., and Vartiainen, E. M., "Quantitative cars spectroscopy using the maximum entropy method: The main lipid phase transition," *ChemPhysChem* **8**(2), 279–287 (2007).
- [11] Masia, F., Glen, A., Stephens, P., Borri, P., and Langbein, W., "Quantitative chemical imaging and unsupervised analysis using hyperspectral coherent anti-stokes raman scattering microscopy," *Anal. Chem.* **85**(22), 10820–10828 (2013).
- [12] Lee, Y. J., Moon, D., Migler, K. B., and Cicerone, M. T., "Quantitative image analysis of broadband cars hyperspectral images of polymer blends," *Anal. Chem.* **83**(7), 2733–2739 (2011).
- [13] Ozeki, Y., Umemura, W., Otsuka, Y., Satoh, S., Hashimoto, H., Sumimura, K., Nishizawa, N., Fukui, K., and Itoh, K., "High-speed molecular spectral imaging of tissue with stimulated raman scattering," *Nature Photon.* **6**, 845–851 (2012).
- [14] Zhang, D., Wang, P., Slipchenko, M. N., Ben-Amotz, D., Weiner, A. M., and Cheng, J.-X., "Quantitative vibrational imaging by hyperspectral stimulated raman scattering microscopy and multivariate curve resolution analysis," *Anal. Chem.* **85**(1), 98–106 (2013).
- [15] Masia, F., Karuna, A., Borri, P., and Langbein, W., "Hyperspectral image analysis for cars, srs, and raman data," *J. Raman Spectrosc.* **46**(8), 727–734 (2015).
- [16] Pope, I., Masia, F., Bradley, J., Ewan, K., Karuna, A., Payne, L., Guschina, I., Harwood, J., Swann, K., Dale, T., Watson, P., Langbein, W., and Borri, P., "Coherent raman scattering microscopy: Technology developments and biological applications," in [2018 20th International Conference on Transparent Optical Networks (ICTON)], 1–4 (2018).
- [17] Karuna, A., Masia, F., Wiltshire, M., Errington, R., Borri, P., and Langbein, W., "Label-Free Volumetric Quantitative Imaging of the Human Somatic Cell Division by Hyperspectral Coherent Anti-Stokes Raman Scattering," *Anal. Chem.* , 10.1021/acs.analchem.8b04706 (2019).
- [18] Di Napoli, C., Pope, I., Masia, F., Langbein, W., Watson, P., and Borri, P., "Quantitative spatiotemporal chemical profiling of individual lipid droplets by hyperspectral cars microscopy in living human adipose-derived stem cells," *Anal. Chem.* **88**(7), 3677–3685 (2016).
- [19] Masia, F., Glen, A., Stephens, P., Langbein, W., and Borri, P., "Label-free quantitative chemical imaging and classification analysis of adipogenesis using mouse embryonic stem cells," *J. Biophot.* **11**(7), e201700219 (2018).

- [20] Masia, F., Pope, I., Watson, P., Langbein, W., and Borri, P., “Bessel-beam hyperspectral cars microscopy with sparse sampling: Enabling high-content high-throughput label-free quantitative chemical imaging,” *Anal. Chem.* **90**(6), 3775–3785 (2018).
- [21] Neumann, B., Walter, T., Hériché, J.-K., Bulkescher, J., Erfle, H., Conrad, C., Rogers, P., Poser, I., Held, M., and Liebel, U., “Phenotypic profiling of the human genome by time-lapse microscopy reveals cell division genes,” *Nature* **464**, 721–727 (2010).
- [22] Zangle, T. A. and Teitell, M. A., “Live-cell mass profiling: an emerging approach in quantitative biophysics,” *Nat. Meth.* **11**(12), 1221–1228 (2014).
- [23] Popescu, G., Park, Y., Lue, N., Best-Popescu, C., Deflores, L., Dasari, R. R., Feld, M. S., and Badizadegan, K., “Optical imaging of cell mass and growth dynamics,” *Am. J. Physiol. Cell Physiol.* **295**(2), C538–C544 (2008).
- [24] Kostyk, P., Phelan, S., and Xu, M., “Cell cycle imaging with quantitative differential interference contrast microscopy,” *Proc. SPIE* **8587**, 8587 (2013).
- [25] Pope, I., Langbein, W., Watson, P., and Borri, P., “Simultaneous hyperspectral differential-cars, tpf and shg microscopy with a single 5 fs ti:sa laser,” *Opt. Express* **21**(6), 7096–7106 (2013).
- [26] Rocha-Mendoza, I., Langbein, W., and Borri, P., “Coherent anti-stokes raman microspectroscopy using spectral focusing with glass dispersion,” *Appl. Phys. Lett.* **93**, 201103 (2008).
- [27] Langbein, W., Rocha-Mendoza, I., and Borri, P., “Coherent anti-stokes raman micro-spectroscopy using spectral focusing: Theory and experiment,” *J. Raman Spectrosc.* **40**, 800–808 (2009).
- [28] Colland, Y. and Kosma, V. M., “Morphometry in cancer diagnosis,” in [*Cancer management in man*], Goldson, A. L., ed., ch. 10, 135, Kluwer Academic Publishers (1989).
- [29] Aknoun, S., Savatier, J., Bon, P., Galland, F., Abdeladim, L., Wattellier, B., and Monneret, S., “Living cell dry mass measurement using quantitative phase imaging with quadriwave lateral shearing interferometry: An accuracy and sensitivity discussion,” *J. Biomed. Opt.* **20**, 126009 (2015).
- [30] Hobro, A. J. and Smith, N. I., “An evaluation of fixation methods: Spatial and compositional cellular changes observed by raman imaging,” *Vib. Spectrosc.* **91**, 31–45 (2017).
- [31] Masia, F., Borri, P., and Langbein, W., “Sparse sampling for fast hyperspectral coherent anti-stokes raman scattering imaging,” *Opt. Express* **22**, 4021 – 4028 (2014).